Saudi Journal of Biological Sciences (2017) **24**, 1344–1354

King Saud University

Saudi Journal of Biological Sciences

www.ksu.edu.sa
www.sciencedirect.com

ORIGINAL ARTICLE

Wake structure and hydrodynamic performance of flapping foils mimicking fish fin kinematics

Weixing Liu [a,1], **Ningyu Li** [a,*,1], **Jinxin Zhao** [b], **Yumin Su** [a]

[a] *Science and Technology on Underwater Vehicle Laboratory, Harbin Engineering University, Harbin 150001, China*
[b] *Beijing Machine and Equipment Institute, Beijing 100854, China*

Received 26 June 2016; revised 1 September 2016; accepted 4 September 2016
Available online 12 September 2016

KEYWORDS

Flapping foil;
Immersed boundary method;
Hydrodynamic performance;
Wake vortex

Abstract Numerical simulations are used to investigate the wake structure and hydrodynamic performance of bionic flapping foils. The study is motivated by the quest to understand the fluid dynamics of fish fins and use it in the underwater propulsion. The simulations employ an immersed boundary method that makes it possible to simulate flows with complex moving boundaries on fixed Cartesian grids. A detailed analysis of the vortex topology shows that the wake of flapping foils is dominated by two sets of complex shaped vortex rings that convect at oblique angles to the wake centerline. The wake of these flapping foils is characterized by two oblique jets. Simulations are also used to examine the wake vortex and hydrodynamic performance over a range of Strouhal numbers and maximum pitch angles and the connection between the foil kinematics, vortex dynamics and force production is discussed. The results show that the variety law of the hydrodynamic performance with kinematic parameters strongly depends on the flow dynamics underlying the force production, including the orientation, interconnection and dissipation rate of the vortex rings.

1. Introduction

Despite impressive innovations in underwater vehicles, both the military and scientific communities hope to benefit from more maneuverable vehicles. Existing underwater vehicles are mostly propelled by the traditional propeller-rudder system and this has shown poor maneuverability performance and low efficiency in unsteady flow. Based on studies about bio-fluid mechanics by Xiao and Zhu (2014) and Zhang et al. (2011), the application of bionic technology in underwater vehicles is becoming a feasible scheme for the improvement. Flapping foil propulsion as a kind of bionic propulsion type is increasingly studied by investigators.

Most of previous studies have assumed that the aspect ratio of the flapping foil is large and have therefore restricted their attention to two-dimensional foils. In Triantafyllou et al. (1992) and Read et al. (2003))'s experimental studies, approximate two-dimensional flow has been accomplished by use of high-aspect-ratio foils and endplates, whereas numerical

* Corresponding author.
E-mail address: liningyu123@aliyun.com (N.Y. Li).
[1] These authors are contributed equally to this work.
Peer review under responsibility of King Saud University.

ELSEVIER Production and hosting by Elsevier

http://dx.doi.org/10.1016/j.sjbs.2016.09.015
1319-562X

studies of Lewin and Haj-Hariri (2003) and Lu and Liao (2006) explicitly perform two-dimensional simulations that ignore any spanwise variability in the foil geometry and the flow field to achieve this.

On the other hand, a number of studies have examined the hydrodynamic performance of finite aspect-ratio flapping foils/wings. Dong et al. (2006) have investigated the effect of aspect ratio on the vortex topology and hydrodynamic performance of thin ellipsoidal foils. Sane and Dickinson (2001) have performed detailed experimental studies with a dynamically scaled mechanical model of the fruit fly to discuss the production of unsteady aerodynamic forces in the influence of wing kinematics, and Sun and Tang (2002) have used this same wing in their numerical simulations to study the lift and power requirements for hovering flight. Techet et al. (2005) have examined the propulsive performance of a three-dimensional flapping foil with an aspect ratio of about 4.5. Li et al. (2009) have studied the hydrodynamic performance of an unsteady flapping foil by a surface panel method over a range of kinematic parameters. Chen (2009) has simulated numerically the unsteady flow field around a flapping wing using the software FLUENT and the effects of different parameters on the thrust performance have been analyzed.

Despite all of these previous works on finite aspect-ratio flapping foils/wings, the number of studies that have systematically examined the connection between the foil kinematics, vortex dynamics and force production underlying the variety law of the hydrodynamic performance with kinematic parameters is rare. Usually, only the two-dimensional section of the vortex structure can be obtained by use of digital particle image velocimetry, and the three-dimensional wake vortex computed from the potential flow panel method ignoring the viscosity of the fluid is different from the reality, especially in the details of the near-field flow. So the research on wake structure and hydrodynamic performance of bionic flapping foils through the use of CFD method is not only theoretically significant but also practically valuable. The immersed boundary method makes it possible to simulate flows with complex moving boundaries on fixed Cartesian grids and has been paid increasing attention in the study of the biofluid mechanics since these researches involve complex geometries and kinematics. In our study, based on the basic idea of the immersed boundary method and advanced CFD techniques, a modified ghost-cell immersed boundary method is proposed. This paper is organized as follows. The calculation model of the flapping foil mimicking fish fin kinematics is first introduced. This is followed by the numerical simulation procedure to be employed, and then the effects of kinematic parameters on the wake topology and hydrodynamic performance and corresponding mechanism analyses.

2. Material and methods

2.1. Computational models

We consider the heaving-pitching motions of a NACA0030 foil at a constant inflow as displayed in Fig. 1. Its chord and span are denoted with C and S, respectively. U is the inflow velocity. The surface of the foil is represented by an unstructured grid with triangular elements and the foil is oriented with the x-axis along the chordwise direction and the z-axis along the spanwise direction. The foil performs heaving-pitching

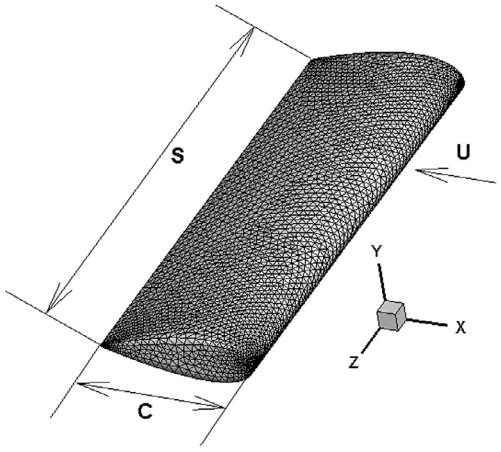

Figure 1 Foil geometry and coordinates.

motions mimicking fish fin kinematics, according to Xiao and Zhu (2014) and Techet et al. (2005).

The heave motion in the y-direction as a function of the time t.

$$h(t) = h_0 \cos(2\pi f t) \tag{1}$$

where h_0 is the maximum amplitude of the heave motion and f is the motion frequency.

The pitch motion is about the foil's 1/4 chord position. The pitch motion is then

$$\theta(t) = \theta_0 \cos(2\pi f t + \psi) \tag{2}$$

where θ_0 is the maximum pitch angle and ψ is the phase shift between heave and pitch. For Read (2000)'s work the motions with a phase shift of 90° are chosen because they lead to good thrust production and efficiency.

The aspect ratio of the foil is defined as

$$AR = S/C \tag{3}$$

For convenience, one key parameter in this study, the Strouhal number, is introduced here, which is defined as

$$St = 2h_0 f/U \tag{4}$$

where $2h_0$ is an estimate of the width of the foil wake. As to the parameter space studied in the experiment of a heaving-pitching foil by Read (2000), $2h_0$ is a valid approximation.

The Reynolds number is defined as

$$\mathrm{Re} = UC/v \tag{5}$$

where v is the kinematic viscosity.

According to the above analysis and the coordinate system, the thrust coefficient is then

$$C_x = F_x/0.5\rho U^2 A_p \tag{6}$$

where ρ is the fluid density, A_p is the projected area of the flapping foil, F_x is the thrust.

The time averaged thrust coefficient is defined as

$$C_{xm} = \frac{1}{T}\int_0^T C_x dt \tag{7}$$

where T is the motion period.

The efficiency of the flapping foil is defined as

$$\eta = \bar{P}_{out}/\bar{P}_{in} \tag{8}$$

where $\bar{P}_{out}$ is the time averaged power output and $\bar{P}_{in}$ is the time averaged power input:

$$\bar{P}_{out} = \frac{1}{T}\int_0^T F_x U dt \tag{9}$$

$$\bar{P}_{in} = -\frac{1}{T}\int_0^T (F_y \dot{h} + M_z \dot{\theta}) dt \tag{10}$$

where F_y is the lift, M_z is the pitch moment, $\dot{h}$ is the heave velocity, and $\dot{\theta}$ is the pitch angular velocity.

2.2. Numerical methods

2.2.1. Governing equations and numerical procedure

The equations governing this flow are the three-dimensional unsteady, incompressible Navier–Stokes equations:

$$\int_{CS} \rho \vec{u} \cdot \vec{n} dS = 0 \tag{11}$$

$$\frac{\partial}{\partial t}\int_{CV} \rho \vec{u} dV + \int_{CS} \rho \vec{u}(\vec{u} \cdot \vec{n}) dS = -\int_{CS} p \vec{n} dS + \int_{CS} \mu \nabla \vec{u} \cdot \vec{n} dS \tag{12}$$

where $\vec{u}$ is the cell-center velocity, p is the pressure, and ρ and μ are the fluid density and dynamic viscosity, respectively. CV and CS denote the control-volume and control-surface, respectively, and $\vec{n}$ is the unit vector normal to the control-surface.

The Navier–Stokes Eq. (11) and Eq. (12) are discretized using a cell-centered, collocated (non-staggered) arrangement of the primitive variables ($\vec{u}$, p). In addition to the cell-center velocity $\vec{u}$ the face-center velocity $\vec{U}$ is computed. In a manner similar to a fully staggered arrangement, as shown in Fig. 2, only the component normal to the cell-face is computed and stored. A second-order accurate fractional step method, a modified variant of the projection method according to Ferziger and Peric (2002), is used for advancing the solution from time level n to $n+1$.

The first sub-step of this method is to solve for an intermediate velocity field using the momentum equations. For the choice of the time-stepping scheme, previously proposed immersed boundary methods mostly employ explicit or semi-implicit schemes, such as methods of Yang and Balaras (2006), Mittal et al. (2008), Iijima et al. (2013) and others. These schemes have to use small time-step size because of the stability restriction, which leads to the increase of computational time. In this paper, the momentum equations are discretized in time using a second-order implicit Crank–Nicolson scheme. This eliminates the stability constraint which can be quite severe in simulation of viscous flows, and large time-step size can be adopted on the premise of the solution accuracy of unsteady problems. The semi-discrete form of the momentum equations for each cell can therefore be written as

$$\int_{CV} \rho \frac{\vec{u}^* - \vec{u}^n}{\Delta t} dV + \frac{1}{2}\int_{CS} \rho[\vec{u}^*(\vec{U}^* \cdot \vec{n}) + \vec{u}^n(\vec{U}^n \cdot \vec{n})] dS = -\int_{CS} p^n \vec{n} dS + \frac{1}{2}\int_{CS} \mu(\nabla \vec{u}^* + \nabla \vec{u}^n) \cdot \vec{n} dS \tag{13}$$

where Δt is the time-step size and $\vec{u}^*$ and $\vec{U}^*$ denote the intermediate cell-center velocity and face-center velocity, respectively. Eq. (13) is a nonlinear algebraic system, for avoiding the direct solution of the nonlinear system and reducing computational effort, a successive substitution approach is proposed. That is, Eq. (13) is first linearized with every component of $\vec{U}^*$ obtained from available $\vec{u}^*$ by computing the linear average of the corresponding direction and held constant, and then the entire linear system is iterated for once using the GMRES (Generalized Minimum RESidual) method before $\vec{U}^*$ is updated for the next iteration, according to Fraysse et al. (2003).

The second sub-step is the pressure correction step:

$$\int_{CV} \rho \frac{\vec{u}^{n+1} - \vec{u}^*}{\Delta t} dV = -\frac{1}{2}\int_{CV} \nabla p' dV \tag{14}$$

where $p' = p^{n+1} - p^n$ is the pressure correction. At $n+1$ time level, the velocity field has to satisfy the integral mass conservation equation:

$$\int_{CS} \rho \vec{U}^{n+1} \cdot \vec{n} dS = 0 \tag{15}$$

This results in the following integral version of Poisson equation for p':

$$\int_{CS} \nabla p' \cdot \vec{n} dS = \frac{2}{\Delta t}\int_{CS} \rho \vec{U}^* \cdot \vec{n} dS \tag{16}$$

The most time-consuming part of executing the above numerical method is solving the Poisson equation. Therefore, for accelerating the convergence, the use of schemes like the multi grid (MG) or Krylov subspace methods is very desirable. However, the presence of the immersed boundaries complicates implementation of the MG method since it is difficult to perform prolongation and restriction near the boundary. Because Krylov subspace methods are developed for general sparse matrices without assuming anything about the structure of the matrix, they are attractive alternatives. No additional complication is posed by the presence of the immersed boundary for these methods. Based on the above considerations, as a kind of Krylov based iterative method, the GMRES method is employed to solve the Poisson equation for pressure correction. Once the pressure correction is obtained by solving Eq. (16), both the cell-center and face-center velocities are updated separately as

$$\vec{u}^{n+1} = \vec{u}^* - \Delta t(\nabla p')_{cc}/2\rho \tag{17}$$

$$\vec{U}^{n+1} = \vec{U}^* - \Delta t(\nabla p')_{fc}/2\rho \tag{18}$$

where cc and fc denote cell-center and face-center, respectively. It should be pointed out that the pressure gradient at the face-center is not simply computed by a linear interpolation of the pressure gradient at the cell-center. For instance with reference to Fig. 2, the pressure gradient of the x-direction at the cell-center is given by

$$(\partial p'/\partial x)_P = (p'_E - p'_W)/2\Delta x \tag{19}$$

where Δx is the cell size of the x-direction. Whereas the same gradient on the east face is computed as

$$(\partial p'/\partial x)_e = (p'_E - p'_P)/\Delta x \tag{20}$$

For non-staggered methods, the above procedure is necessary to eliminate odd–even decoupling that leads to large pressure variations in space. The idea of separately computing the

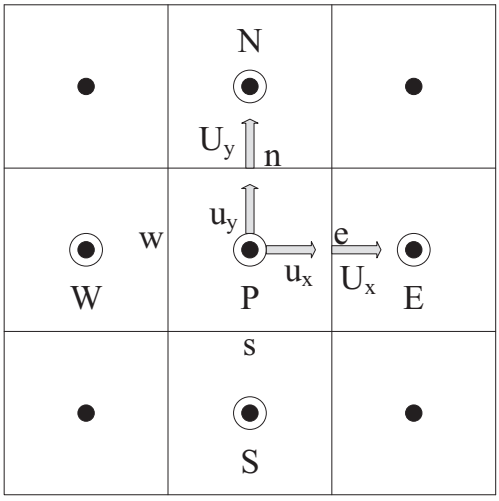

Figure 2 Schematic showing the naming convention and location of cell-center and face-center velocities.

face-center velocities was initially proposed by Zang et al. (1994). When the pressure correction Eq. (16) is discretized in terms of the pressure gradients on the cell faces and the face-center velocity is separately updated as shown in Eq. (18), exact satisfaction of Eq. (15) is guaranteed.

2.2.2. *Immersed boundary treatment*

A multi-dimensional ghost-cell methodology is employed to incorporate the effect of the immersed boundary on the flow. This method falls into the category of "discrete forcing" immersed boundary methods, according to Mittal and Iaccarino (2005).

2.2.2.1. Geometric representation of immersed boundary. Most researches about biofluid mechanics involve complex geometries and kinematics, so the developed method is aimed at simulating flows over arbitrarily complex 3D immersed stationary and moving boundaries. The unstructured mesh with triangular elements is chosen to represent the surface of the immersed boundary. This geometric representation is very fit for the wide variety of biological flow configurations since it is flexible enough so as not to limit the type of geometries that can be handled. The surface of the flapping foil represented by triangulation is shown in Fig. 1. The unstructured surface grid of the flapping foil is then "immersed" into the Cartesian volume mesh of the flow field, as depicted in Fig. 3.

2.2.2.2. Identification of cell type. The method proceeds by first identifying cells of which nodes are inside the solid boundary and cells of which nodes are outside the solid boundary. As shown in Fig. 4, for a given node, a straight forward approach is to determine the triangular element closest to the given node and taking a dot-product of the vector $\vec{r}$ extending from this element to the node, with the unit vector normal to this element $\hat{n}$. That the node is outside (inside) the solid boundary is then implied by a positive(negative) value of the dot-product $\vec{r} \cdot \hat{n}$.

Based on the solid–fluid demarcation, the cells in the flow field can be divided into three categories. First is the category of "fluid cells" whose nodes are outside the solid boundary. The second category consists of so-called "ghost-cells" of

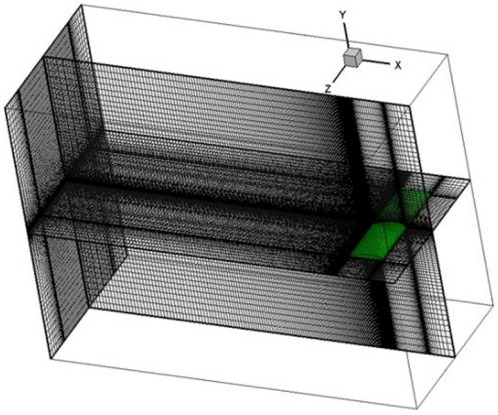

Figure 3 Mesh model of the flow field with immersed boundary.

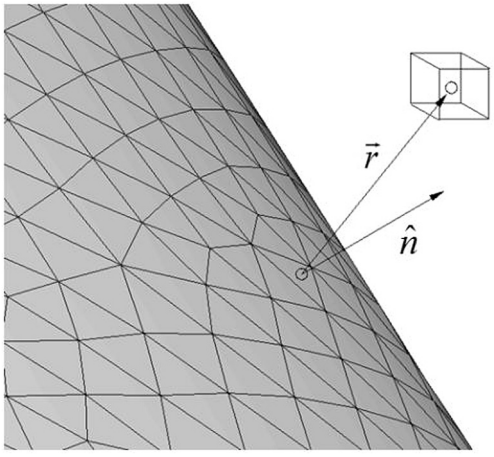

Figure 4 Schematic describing the procedure for determining whether a node is inside or outside the solid boundary.

which nodes are inside the solid but have at least one neighbor in the fluid. Third is the category of "solid cells". These are cells whose nodes are inside the solid and have no neighbor in the fluid. The schematic in Fig. 5 shows the three types of cells for a solid boundary cutting through a Cartesian grid.

2.2.2.3. Reconstruction scheme of boundary condition. The overall method now is to establish an appropriate equation for ghost-cells which ensures the implicit satisfaction of the boundary condition on the immersed boundary in the vicinity of each ghost-cell.

We express the local flow variable φ in terms of a polynomial and employ it to derive the value at the ghost-cell. The accuracy depends on the degree of the polynomial. Although polynomials of higher degree are deemed to be more accurate, numerical instability and boundedness problems often occur with the use of them. Additionally, in the light of previous studies of LeVeque and Oliger (1983) and Tseng and Ferziger (2003), the use of an approximation of one order lower accuracy at the boundary does not reduce the overall accuracy of the scheme. In order to minimize the probability of numerical instability and save computational time, the linear reconstruction scheme is employed.

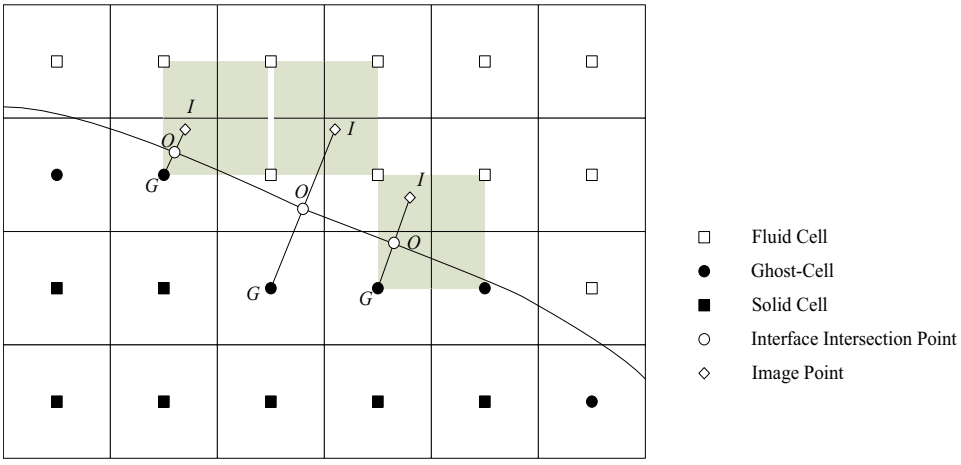

Figure 5 Schematic showing ghost-cell methodology employed in the current solver.

As shown in Fig. 5, a line segment is extended from the node of ghost-cells into the fluid to an image point I such that the interface intersection point O is midway between the ghost-node G and the image point. The point O is the point at which the boundary condition is to be satisfied. In the current solver, O is chosen as the center of the triangular element closest to it to keep from additional complications. A linear interpolation in 3D is

$$\varphi = b_0 + b_1 x + b_2 y + b_3 z \tag{21}$$

The image point value is a weighted combination of the values at the interface intersection point and three of the eight nodes surrounding the image point. In terms of the nodal values, the coefficients can be expressed as:

$$\begin{bmatrix} b_0 \\ b_1 \\ b_2 \\ b_3 \end{bmatrix} = A^{-1} \begin{bmatrix} \varphi_0 \\ \varphi_1 \\ \varphi_2 \\ \varphi_3 \end{bmatrix} \tag{22}$$

where A is a 4×4 matrix. For Dirichlet boundary condition that is employed for the velocity, the elements of matrix A can be computed from the coordinates of the four points as

$$A = \begin{bmatrix} 1 & x_0 & y_0 & z_0 \\ 1 & x_1 & y_1 & z_1 \\ 1 & x_2 & y_2 & z_2 \\ 1 & x_3 & y_3 & z_3 \end{bmatrix} \tag{23}$$

Once the coefficients are determined from Eq. (22), using Eq. (21) at the image point, a final expression for the variable at the image point is given by

$$\varphi_I = \sum_{j=0}^{3} \alpha_j \varphi_j \tag{24}$$

In the above equation, α's depend on b'sand the coordinates of the image point. Following this, the value of variable at the ghost-cell is expressed as a linear approximation along the line segment which incorporates the prescribed boundary condition at the interface intersection point:

$$\varphi_G = 2\varphi_O - \varphi_I \tag{25}$$

During the solution process, the above formula for the ghost-cell is written in the following implicit form by use of Eq. (24):

$$\varphi_G + \sum_{j=0}^{3} \alpha_j \varphi_j = 2\varphi_O \tag{26}$$

There is an advantage to introducing the image point into the reconstruction scheme. If the ghost-node value is directly obtained by extrapolation from the values at the fluid nodes and interface intersection point, large negative weighting coefficients will be encountered when the interface intersection point is close to one of the fluid nodes used in the extrapolation. Although algebraically correct, this can lead to numerical instability.

The reconstruction scheme is robust enough to tackle a variety of situations. For instance, a case may be encountered where one of the eight nodes surrounding the image point is the node of the ghost-cell itself(see the left ghost-cell in Fig. 5). This case does not cause any additional problems since three of other seven nodes along with the interface intersection point can be chosen as the interpolation stencil. It may also be the situation that the eight nodes surrounding the image point for a given ghost-cell contains nodes of other ghost-cells (see the right ghost-cell in Fig. 5). In this situation, if the number of the fluid nodes N among the eight nodes surrounding the image point is greater than or equal to three, three of the N fluid nodes along with the interface intersection point can be chosen as the interpolation stencil. If not, the interpolation stencil consists of the N fluid nodes, the interface intersection point and $3 - N$ other ghost-nodes. Although the latter does imply that some of the ghost-node values are coupled to each other, it does not lead to any consistency issues since the equation for the ghost-cell is solved in a fully coupled manner with the governing Eqs. (13) and (16) for the surrounding fluid cells along with the equations for other ghost-cells.

A similar scheme can be employed for Neumann boundary condition that is used for the pressure correction. The only difference is in the construction of matrix A in Eq. (22). This makes the current scheme applicable to kinds of boundary conditions. The normal derivative of the pressure correction on the boundary can be expressed as

$$\partial p'/\partial n = (\partial p'/\partial x)\hat{n}_x + (\partial p'/\partial y)\hat{n}_y + (\partial p'/\partial z)\hat{n}_z \tag{27}$$

where $\hat{n}_x$, $\hat{n}_y$ and $\hat{n}_z$ are the components of the unit vector normal to the boundary. Since we know the geometry of the immersed boundary, $\hat{n}_x$, $\hat{n}_y$ and $\hat{n}_z$ are known. Differentiation of Eq. (21) yields

$$\partial p'/\partial x = b_1, \partial p'/\partial y = b_2, \partial p'/\partial z = b_3 \tag{28}$$

Linear reconstruction requires the interface intersection point and three of the eight nodes surrounding the image point. Finally, the coefficients can be obtained as follows:

$$\begin{bmatrix} b_0 \\ b_1 \\ b_2 \\ b_3 \end{bmatrix} = A^{-1} \begin{bmatrix} \partial p'/\partial n \\ p'_1 \\ p'_2 \\ p'_3 \end{bmatrix} \tag{29}$$

The elements of matrix A can be evaluated from the coordinates of the three points and the components of the unit vector normal to the boundary as

$$A = \begin{bmatrix} 0 & \hat{n}_x & \hat{n}_y & \hat{n}_z \\ 1 & x_1 & y_1 & z_1 \\ 1 & x_2 & y_2 & z_2 \\ 1 & x_3 & y_3 & z_3 \end{bmatrix} \tag{30}$$

2.2.2.4. Moving boundary. In the moving boundary case, we need move the immersed boundary from its current location to the new location at every time step. This is achieved by moving the nodes of the surface triangles with a known velocity. Thus we use the following formula to update the position of a surface element vertex:

$$\vec{p}^{n+1} = \vec{p}^{n} + \vec{v}^{n+1}\Delta t \tag{31}$$

where $\vec{p}$ is the position vector of the vertex and $\vec{v}$ is the vertex velocity.

In the above section, the reconstruction scheme of the boundary condition is discussed. This procedure is stable, robust and efficient. The scheme is equally applicable to both stationary and moving boundaries. In the case of moving boundaries, the interface intersection points, image points and weighted coefficients must be recomputed at every time step but the reconstruction scheme is not affected by this.

One problem associated with moving boundaries is the so-called "fresh cell" issue according to Mittal et al. (2008). This refers to the case where a cell that is in the solid emerges into the fluid at the next time-step (or, vice versa) due to boundary motion. Plotted in Fig. 6 is the emergence of two fresh cells caused by boundary motion from time level n to $n+1$. For a fresh cell, some of the required values from the previous time-step are not physical because of the fact that the boundary changes locations. For the explicit or semi-implicit time-stepping schemes, due to the CFL restriction, the boundary cannot move by more than one cell deep in each sub-step. In this situation, Yang and Balaras (2006) have employed a field-extension methodology, and a procedure of constructing the interpolation stencil by use of the normal probe has been proposed by Mittal et al. (2008). But when the implicit time-stepping scheme is employed, the layer of fresh cells may be more than one gird cell. In the current solver, a new methodology combining the modified Shepard interpolation according to Thacker et al. (2010) and successive substitution is proposed. In the methodology, the required values of fresh cells from the previous time-step are first obtained from available values of surrounding fluid cells using the modified Shepard interpolation and held constant. This is followed by the solution of Eq. (13), and then the required values of fresh cells from the previous time-step are updated for the next iteration. Since the modified Shepard algorithm for interpolation of scattered data is employed, the proposed methodology is

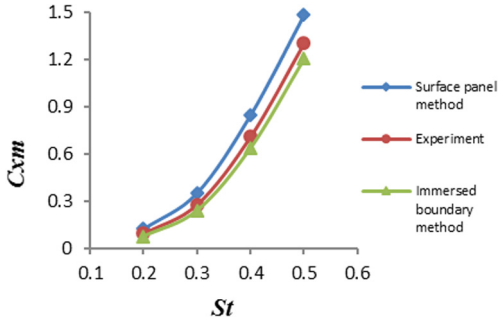

Figure 7 Time averaged thrust coefficient as a function of Strouhal number.

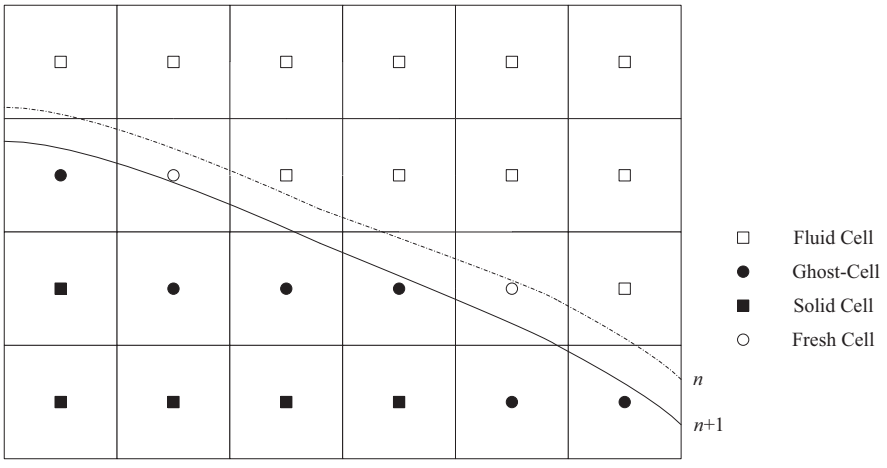

Figure 6 Schematic describing the appearance of fresh cells due to boundary motion.

enough flexible to deal with various complex moving boundaries.

3. Results

3.1. Validation of numerical method

In order to verify the calculation method used in this study, the numerical results from the immersed boundary method are compared with the experimental results of Read (2006) and the numerical results from a surface panel method developed by Li et al. (2012). With the parameters of $AR = 3$, $\mathrm{Re} = 1000$, $St = 0.2 - 0.5$, $h_0/C = 0.5$ and $\theta_0 = 5°$, the variation of the time averaged thrust coefficient with Strouhal number is shown in Fig. 7. For the entire range of Strouhal numbers varied, it can be seen that the variation trends of the calculation results from the immersed boundary method and surface panel method are consistent with the experimental results. The time averaged thrust increases with the Strouhal number. Because the fluid viscosity is considered, the immersed boundary method can calculate the hydrodynamic force of the flapping foil in real environment more accurately than the surface panel method.

3.2. Wake structure

The focus in this section is to provide a comprehensive description of the wake structure. Vortices in three-dimensional simulations are identified by plotting an isosurface of Q, the second invariant of the velocity gradient tensor, known as the Q criterion, according to Hunt et al. (1988). A positive value of Q is a measure for any excess of rotation rate with respect to the strain. Therefore, the flow exhibit a swirling motion within a region where $Q > 0$ as shown by Chakraborty et al. (2005). For this analysis, we focus on the case with $AR = 1.5$, $\mathrm{Re} = 200$, $St = 0.5$, $h_0/C = 0.5$ and $\theta_0 = 30°$.

Fig. 8(a), (b) and (c) shows perspective, side and top views of the wake topology for this situation at a phase when the foil is at the lowest point in its heaving cycle. The downstream wake of the foil consists of two sets of complex shaped vortex rings which propagate at oblique angles to the wake center line. We identify rings R_2 in the lower set and R_1 in the upper set and indicate their direction of rotation by lines and arrows. Here too we find that the wake tends to become slightly narrower in the z-direction and to diverge in the$y$-direction. The mechanism of this phenomenon can be understood by

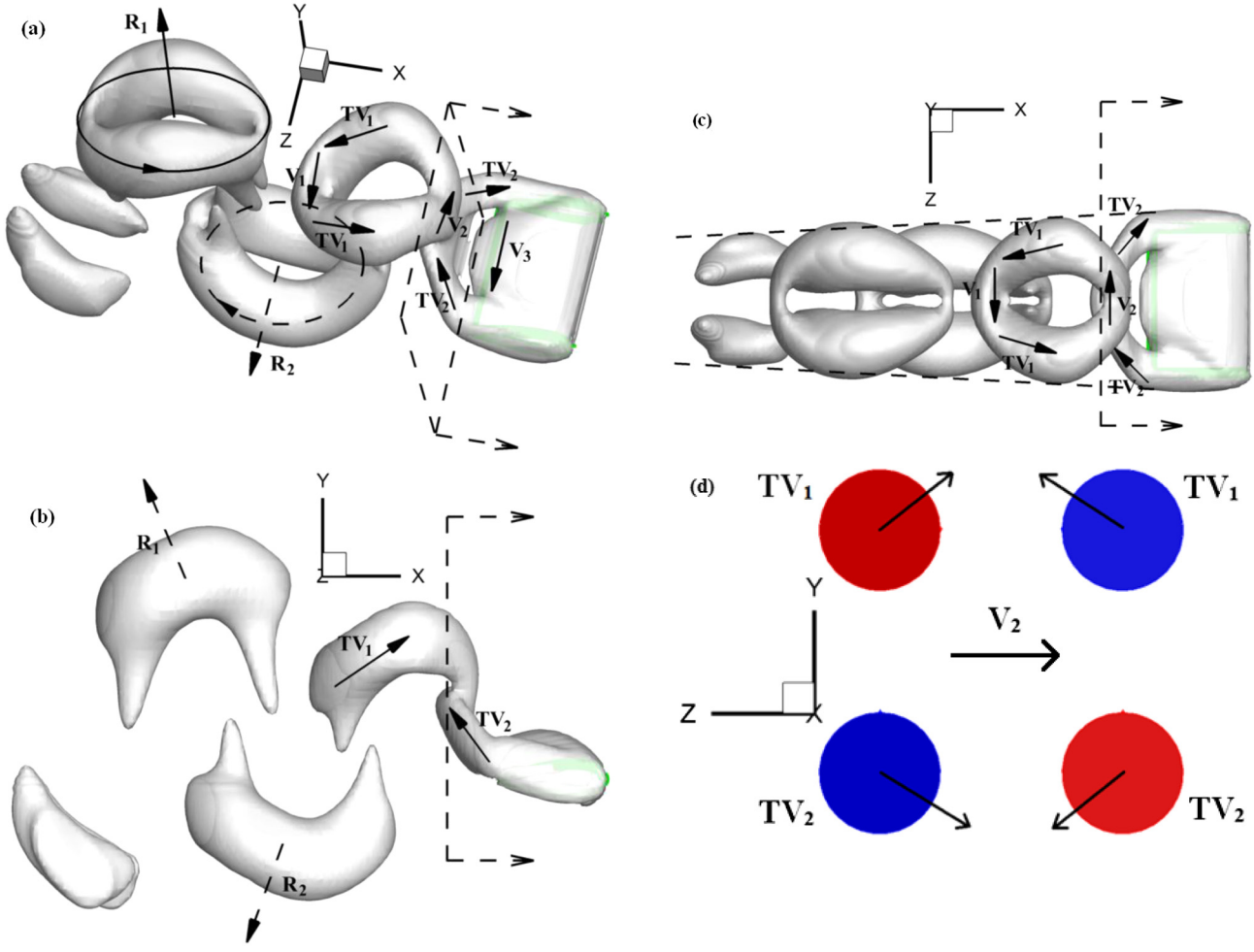

Figure 8 Wake topology at the phase where the foil is at the lowest point in its heaving cycle.(a) Perspective view. (b) Side view. (c) Top view. (d) Front-view schematic of tip vortices on streamwise plane indicated in (a), (b) and (c).The red-color vortices are outward, whereas the blue-color vortices are inward.

examining flow on the streamwise plane in this region as indicated in Fig. 8(a), (b) and (c) by the dashed line. A schematic of the tip vortices TV_1 and TV_2 and spanwise vortex V_2 on this plane is plotted in Fig. 8(d). The direction of the velocity induced on one tip vortex by the other three is represented by the arrow and this indicates that the vortices in the same system will tend to move towards each other, which leads to the slight narrowing of the wake in the z-direction. Fig. 8(d) also clearly shows that the tip vortices in one ring will tend to move away from the tip vortices of the adjoining ring, which leads to the diverging of the wake in the y-direction. In the investigation of thin ellipsoidal foils by Dong et al. (2006), a similar mechanism has also been gained. The upward motion of vortex V_1 induced by the tip vortices is the primary mechanism that causes the inclination of the vortex ring. Once the ring is inclined, its self-induced velocity tends to convect it along its axis, which then explains the convection of the vortex rings at an oblique angle to the wake centerline.

4. Discussion

4.1. Effect of Strouhal number on wake topology and hydrodynamic performance

In this section, we examine the effect of Strouhal number on the vortex topology and hydrodynamic performance and for this analysis, Strouhal numbers are varied from $St = 0.35 - 1.1$. Other parameters for this simulation are: $AR = 1.5$, $\mathrm{Re} = 200$, $h_0/C = 0.5$ and $\theta_0 = 30^\circ$.

Fig. 9 presents the vortex topology for $St = 0.35$ and 0.95 for the foil and this can be examined in conjunction with the corresponding plot for the $St = 0.5$ case in Fig. 8. In Fig. 9 (a) and (b) where $St = 0.35$, the salient feature is the absence of some linkage between the tip vortices as seen for $St = 0.5$. This makes sense because the tip vortices formed at this lower Strouhal number have lower strength and this weakens the mutual induction mechanism that is responsible for the linking of the tip vortices as described in Section 4.2. When Strouhal number is increased to 0.5 (Fig. 8), the tip vortices link together to form spanwise oriented vortex filaments. Hairpin-like legs can be seen connecting the two vortex trains. As Strouhal number is further increased to 0.95 (Fig. 9(c) and (d)), the vortex rings in the wake become more oriented in the streamwise direction, and they develop more complex hairpin-like legs. Clearly, with increasing Strouhal number, there is a concomitant increase in the tip-vortex strength and their mutual induction leading to the wake becoming wider.

Fig. 10 shows the variation of the time averaged thrust coefficient and efficiency with Strouhal number. The thrust increases monotonically with the Strouhal number. This is because the inclined angle of the vortex rings changes wherein the vortex rings become more erect with increasing Strouhal number and this increases the streamwise momentum of the jet which is directly proportional to the thrust produced by the foil. As the Strouhal number increases, the efficiency increases at first. This is due to larger thrust at higher Strouhal numbers. However, the efficiency decreases after reaching the peak at about $St = 0.8$. This is because the vortex structures in the downstream become more complicated with increasing Strouhal number due to the appearing of more interconnec-

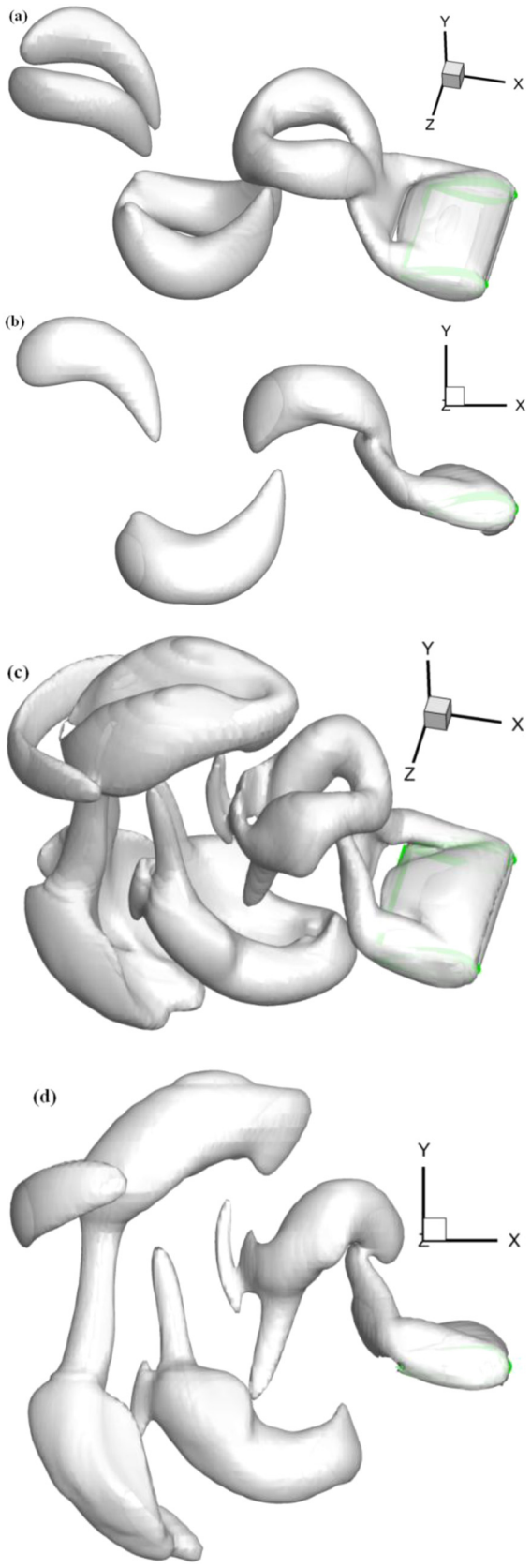

Figure 9 Vortex topology for different Strouhal numbers. The foil is at the lowest point in its heaving cycle. (a) Perspective view for $St = 0.35$. (b) Side view for $St = 0.35$. (c) Perspective viewfor $St = 0.95$. (d) Side view for $St = 0.95$.

tions between the two sets of vortex rings, which leads to the more viscous cancelation of opposite signed vorticity.

4.2. Effect of maximum pitch angle on wake topology and hydrodynamic performance

In this section, the effect of maximum pitch angle on the vortex topology and hydrodynamic performance is discussed. The simulations are carried out with $AR = 1.5$, $\mathrm{Re} = 200$, $St = 0.5$ and $h_0/C = 0.5$ in the case of different maximum pitch angles.

Fig. 11 presents the vortex topology for $\theta_0 = 10^\circ$ and 40° for the foil and this can be examined in conjunction with the corresponding plot for the $\theta_0 = 30^\circ$ case in Fig. 8. As the maximum pitch angle increases, the vortex rings in the wake become more oriented in the streamwise direction and this increases the streamwise momentum of the jet. On the other hand, the vortex rings diffuse more rapidly with increasing maximum pitch angle so that the far downstream vortex ring has disappeared for the $\theta_0 = 40^\circ$ case.

Fig. 12 shows the variation of the time averaged thrust coefficient and efficiency with maximum pitch angle. As the maximum pitch angle increases, the thrust increases at first.

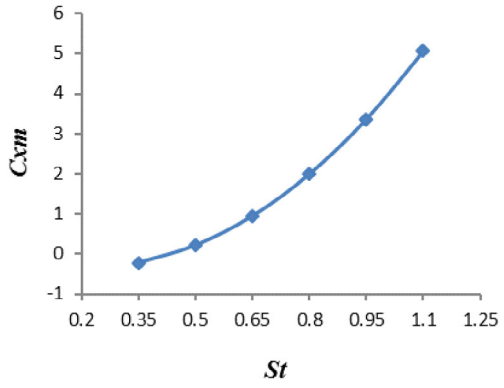

(a)

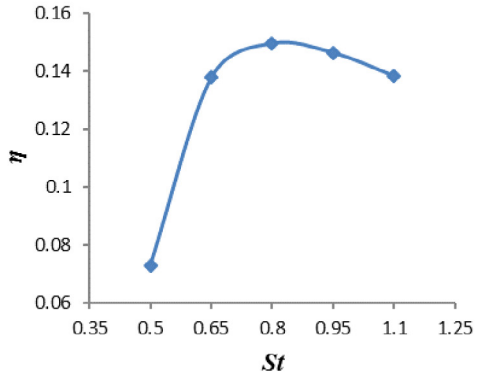

(b)

Figure 10 Hydrodynamic performance for different Strouhal numbers. (a) Time averaged thrust coefficient. (b) Efficiency.

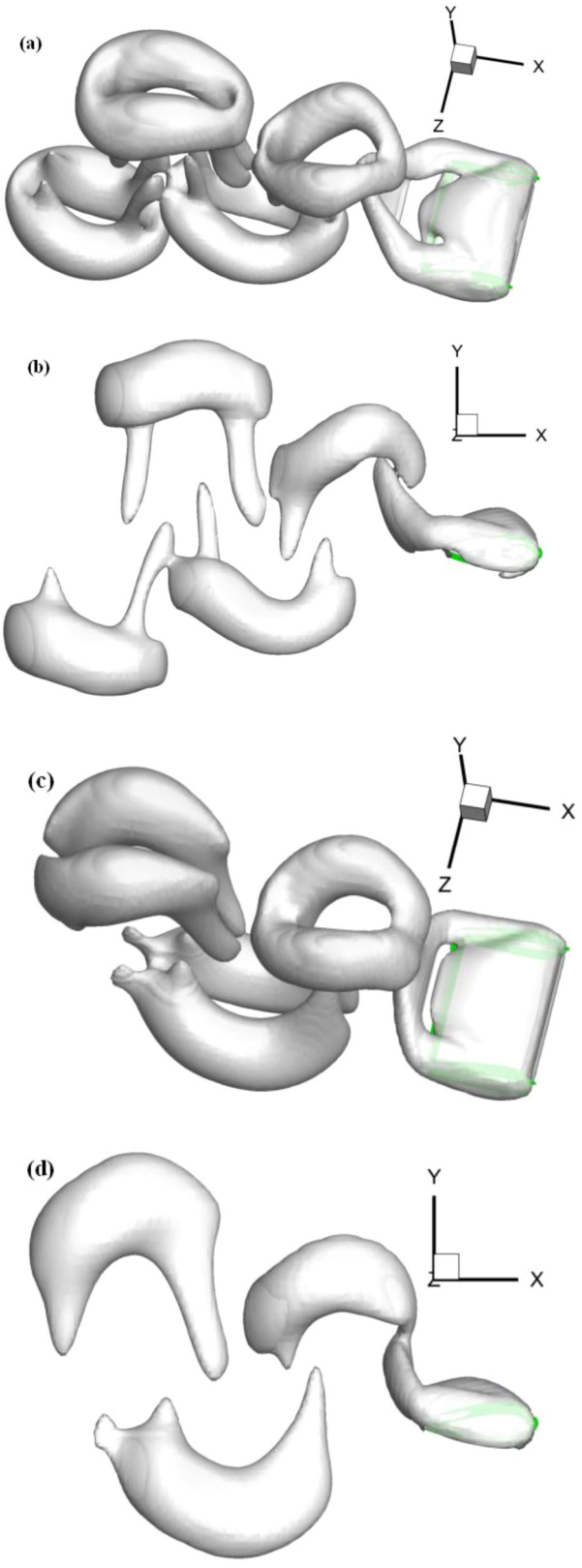

Figure 11 Vortex topology for different maximum pitchangles. The foil is at the lowest point in its heaving cycle. (a) Perspective view for $\theta_0 = 10^\circ$. (b) Side view for $\theta_0 = 10^\circ$. (c) Perspective view for $\theta_0 = 40^\circ$. (d) Side view for $\theta_0 = 40^\circ$.

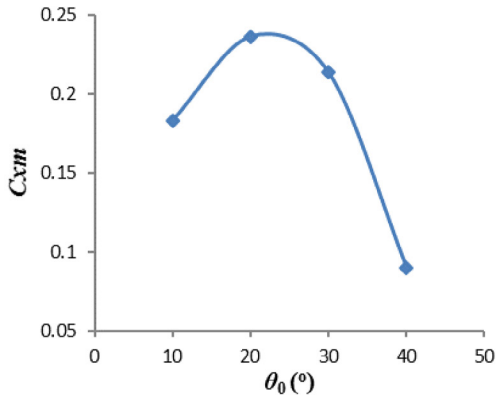

(a)

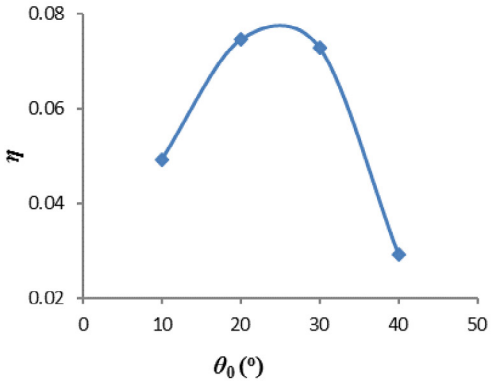

(b)

Figure 12 Hydrodynamic performance for different maximum pitch angles. (a) Time averaged thrust coefficient. (b) Efficiency.

This makes sense since the streamwise momentum of the jet increases. The maximum is reached at a maximum pitch angle of about 20° and then a decreasing thrust is seen. This is because of the rapider dissipation of the vortex rings in the wake. Similar to the thrust, as the maximum pitch angle increases, originally an increasing efficiency is seen which peaks at a maximum pitch angle of between 20° and 30°, and then the efficiency decreases.

5. Conclusions

Numerical simulations of flow past flapping foils mimicking fish fin kinematics have been carried out by use of an immersed boundary solver. The current study is an effort to understand the wake structure and hydrodynamic performance of low-aspect-ratio flapping foils. The following conclusions can be drawn based on the above discussion:

(1) The immersed boundary method adopted in this paper can simulate the unsteady motion of bionic flapping foils quite well.
(2) The vortex topology of the foil consists of two sets of complex shaped vortex rings that propagate at oblique angles to the wake center line. The wake tends to become slightly narrower in the spanwise direction and to open in the vertical direction. The flow downstream of the foil is characterized by two oblique jets of which the streamwise momentum is directly associated with the thrust produced by the foil.
(3) As the Strouhal number increases, the vortex rings become more erect, accompanied by the appearing of more interconnections between two vortex trains, and the wake gets wider. The thrust becomes larger with increasing Strouhal number and this leads to the early augmentation of the efficiency. However, the efficiency decreases after attaining the maximum at a Strouhal number of about 0.8 with the more viscous cancelation of opposite signed vorticity.
(4) As the maximum pitch angle increases, the vortex rings in the wake become more oriented in the streamwise direction and diffuse more rapidly. Both the thrust and efficiency increase firstly, and then decreases with increasing maximum pitch angle.

Conflict of interests

The authors declare that there is no conflict of interests.

Acknowledgment

This work is supported by the National Natural Science Foundation of China (Grant No. 51479039).

References

Chakraborty, P., Balachandar, S., Adrian, R.J., 2005. On the relationships between local vortex identification schemes. J. Fluid Mech. 535, 189–214.
Chen, W.K., 2009. Propulsion Performance Analysis of Flapping Wing based on the CFD (Master thesis). Harbin Engineering University, China (in Chinese).
Dong, H., Mittal, R., Najjar, F.M., 2006. Wake topology and hydrodynamic performance of low-aspect-ratio flapping foils. J. Fluid Mech. 566, 309–343.
Ferziger, J.H., Peric, M., 2002. Computational methods for fluid dynamics. Springer-Verlag, Berlin/Heidelberg/New York.
Fraysse, V., Giraud, L., Gratton, S., Langou, J., 2003. A set of GMRES routines for real and complex arithmetics on high performance computers. CERFACS Technical Report TR/PA/03/3, CERFACS, Toulouse, France.
Hunt, J. C. R., Wray, A. A., Moin, P., 1988. Eddies, stream, and convergence zones in turbulent flows. Cent. Turbulence Res. Rep. No. CTR-S88, Center for Turbulence Research, Stanford, USA, pp. 193–208.
Iijima, A., Sato, T., Tagawa, T., 2013. Numerical analysis of flow around a moving object by an immersed boundary method with the level set method Adv. Mech. Eng. 868240.
LeVeque, R.J., Oliger, J., 1983. Numerical-methods based on additive splittings for hyperbolic partial-differential equations. Math. Comp. 40, 469–497.
Lewin, G.C., Haj-Hariri, H., 2003. Modelling thrust generation of a two-dimensional heaving airfoil in a viscous flow. J. Fluid Mech. 492, 339–362.
Li, Y.L., Wang, Z.L., Su, Y.M., Qin, Z.B., 2009. Hydrodynamic performance of an unsteady flapping foil. J. Hrb. Eng. Univ. 30, 1339–1343 (in Chinese).
Li, N.Y., Su, Y.M., Wang, Z.L., Zhang, X., 2012. Computation method of propulsive efficiency of a three-dimensional flapping foil. J. Shanghai Jiaotong Univ. 46, 323–328 (in Chinese).

Lu, X.Y., Liao, Q., 2006. Dynamic responses of a two-dimensional flapping foil motion. Phys. Fluids 18, 098104.

Mittal, R., Iaccarino, G., 2005. Immersed boundary methods. Annu. Rev. Fluid Mech. 37, 239–261.

Mittal, R., Dong, H., Bozkurttas, M., Najjar, F., Vargas, A., Von Loebbeck, A., 2008. A versatile sharp interface immersed boundary method for incompressible flows with complex boundaries. J. Comput. Phys. 227, 4825–4852.

Read, D.A., 2000. Oscillating Foils for Propulsion and Maneuvering of Ships and Underwater Vehicles (Master thesis). Mass. Inst. Tech., USA.

Read, M.B., 2006. Performance of Biologically Inspired Flapping Foils (Master thesis). Mass. Inst. Tech., USA.

Read, D.A., Hover, F.S., Triantafyllou, M.S., 2003. Forces on oscillating foils for propulsion and maneuvering. J. Fluid Struct. 17, 163–183.

Sane, S.P., Dickinson, M.H., 2001. The control of flight force by a flapping wing: lift and dragproduction. J. Esp. Biol. 204, 2607–2626.

Sun, M., Tang, J., 2002. Lift and power requirements of hovering flight in drosophila virilis. J. Esp. Biol. 205, 2413–2427.

Techet, A. H., Lim, K. L., Hover, F. S., Triantafyllou, M. S., 2005. Hydrodynamic performance of a biologically inspired three-dimensional flapping foil. Proc. of the 14th International Symp. on Unmanned Untethered Submers. Tech. Durham, New Hampshire.

Thacker, W. I., Zhang, J., Watson, L. T., Birch, J. B., Iyer, M. J., Berry, M. W., 2010. Algorithm 905: SHEPPACK: modified Shepard algorithm for interpolation of scattered multivariate data. ACM Trans. Math. Softw.37.

Triantafyllou, G.S., Triantafyllou, M.S., Grosenbaugh, M.A., 1992. Optimal thrust development in oscillating foils with applications to fish propulsion. J. Fluid Struct. 7, 204–224.

Tseng, Y.H., Ferziger, J.H., 2003. A ghost-cell immersed boundary method for flowin complex geometry. J. Comp. Phys. 192, 593–623.

Xiao, Q., Zhu, Q., 2014. A review on flow energy harvesters based on flapping foils. J. Fluid Struct. 46, 174–191.

Yang, J.M., Balaras, E., 2006. An embedded-boundary formulation for large-eddy simulation of turbulent flows interacting with moving boundaries. J. Comput. Phys. 215, 12–40.

Zang, Y., Streett, R.L., Koseff, J.R., 1994. A non-staggered fractional step method for time-dependent incompressible Navier-Stokes equations in curvilinear coordinates. J. Comput. Phys. 114, 18–331994.

Zhang, X., Su, Y.M., Wang, Z.L., 2011. Numerical and experimental studies of influence of the caudal fin shape on the propulsion performance of a flapping caudal fin. J. Hyd. 23, 325–332.